Research Square

Preprints are preliminary reports that have not undergone peer review.
They should not be considered conclusive, used to inform clinical practice,
or referenced by the media as validated information.

Electro-optic frequency comb generation in lithium niobate photonic crystal Fabry-Perot micro-resonator

HYEON HWANG
Korea Advanced Institute of Science and Technology
Seokjoo Go
Korea Advanced Institute of Science and Technology
Guhwan Kim
Electronics and Telecommunications Research Institute
Hong-Seok Kim
Electronics and Telecommunications Research Institute
Kiwon Moon
Electronics and Telecommunications Research Institute
Jung Jin Ju
Electronics and Telecommunications Research Institute
Hansuek Lee
Korea Advanced Institute of Science and Technology
Min-Kyo Seo
minkyo_seo@kaist.ac.kr

Korea Advanced Institute of Science and Technology

Article

Keywords:

Posted Date: October 25th, 2025

DOI: https://doi.org/10.21203/rs.3.rs-7743082/v1

License: This work is licensed under a Creative Commons Attribution 4.0 International License.
Read Full License

Additional Declarations: No competing interests reported.

Electro-optic frequency comb generation in lithium niobate photonic crystal Fabry-Perot micro-resonator

HYEON HWANG,[1,a)] Seokjoo Go,[1] Guhwan Kim,[2] Hong-Seok Kim,[2] Kiwon Moon,[2] Jung Jin Ju,[2] Hansuek Lee,[1] and Min-Kyo Seo[1,b)]

[1]*Department of Physics, Korea Advanced Institute of Science and Technology (KAIST), Daejeon, 34141, Rep. of Korea*

[2]*Electronics and Telecommunication Research Institute (ETRI), Daejeon, 34129, Rep. of Korea*

a) e-mail: hyeon_hwang@kaist.ac.kr

b) e-mail: minkyo_seo@kaist.ac.kr

Abstract:

Integrated electro-optic (EO) combs offer compelling advantages in stability and tunability, but their performance has been constrained by weak modulation efficiency, parasitic Raman scattering, and the difficulty of achieving broad bandwidth within a compact footprint. We demonstrate EO frequency comb generation in a dispersion-engineered photonic crystal Fabry–Pérot (PhC-FP) micro-resonator in thin-film lithium niobate. Hundreds of standing-wave resonant modes with quality factors exceeding 10^6 are supported within a photonic bandgap, while Raman-scattering bands are excluded. Integrated dispersion, primarily shaped by PhC reflectors, includes the zero-dispersion point for phase-matched EO modulation. Consequently, Raman-free EO combs are achieved under high on-chip pump powers of up to 200 mW. Comb characteristics are reconfigurable via microwave power, frequency detuning, and pump wavelength. This platform offers a compact, chip-integrated solution that provides broadband generation, high-power operation, and reconfigurability for EO comb sources in nonlinear and quantum photonic systems.

1. Introduction

Optical frequency combs underpin a broad range of applications in optical communications, precision metrology, LiDAR, and spectroscopy.[1–5] Whereas mode-locked lasers and Kerr microcombs have long been the workhorses for broadband combs, electro-optic (EO) frequency combs offer complementary advantages: deterministic operation, broad electrical tunability, and intrinsically low phase noise with a direct interface to microwave electronics.[6–10] These properties enable stable and reconfigurable operation without the soliton initiation procedures or stringent thermal stabilization often required in Kerr platforms, making EO combs especially attractive for coherent transceivers, frequency synthesis, and emerging quantum-photonic systems.[9]

Thin-film lithium niobate (TFLN) has recently established itself as a premier substrate for integrated EO photonics by combining strong second-order nonlinearity, low-loss waveguides, tight optical confinement, and efficient RF–optical field overlap.[7,11–24] In cavity-enhanced configurations, matching the microwave drive to the optical free-spectral range (FSR) provides resonant gain for sideband generation and access to large, coherent spectral spans with modest RF power. Alongside device advances, there is growing emphasis on programmability: EO comb spectra and temporal waveforms can be engineered by co-designing dispersion, electrode geometry, drive frequency, and modulation index, and by exploiting detuning as a control knob.[10,25,26] This broader perspective motivates EO comb sources that balance three goals simultaneously: wide optical bandwidth, coherence/phase stability, and high optical power.

Meeting all three goals on TFLN remains challenging. A central constraint is parasitic stimulated Raman scattering that can emerge under strong intracavity fields, transferring pump power out of the EO sideband ladder and degrading coherence.[27–32] In conventional traveling-wave resonators (e.g., microrings and racetracks), the broad set of high-Q modes often overlaps Raman-active spectral regions. Furthermore, device orientations and polarizations chosen to maximize the relevant χ^2 tensor components can avoidably enhance Raman gain.[30] Unlike Kerr comb, where dispersion engineering or tailored cavity loss can shift or suppress Raman processes, EO combs are externally driven at fixed microwave frequencies, so many of those mitigation strategies do not translate directly.[33,34] These considerations point to the need for new cavity topologies that combine (i) fine dispersion control for phase-matched EO modulation with (ii) spectral selectivity that inherently avoids Raman-susceptible bands.

This work introduces an EO frequency-comb platform based on a dispersion-engineered photonic-crystal Fabry–Pérot (PhC-FP) micro-resonator in TFLN. By employing PhC reflectors, we selectively support standing-wave resonant modes with high Q factors within the photonic bandgap, while inherently excluding the spectral range of parasitic Raman scattering. The PhC reflectors shape integrated dispersion and photonic bandgap to include the zero-dispersion point and facilitate phase-matched EO modulation in a compact footprint. We experimentally demonstrate high-power EO comb generation, supporting over ~650 resonant modes with intrinsic Q factors exceeding 10^6 and Raman-free operation even under on-chip pump powers up to 200 mW. We further demonstrate dynamic control over comb characteristics through modulation strength, frequency detuning, and dispersion engineering, with measurements in excellent agreement with theoretical predictions.

2. EO frequency comb generation in the dispersion-engineered PhC FP micro-resonator

Figure 1a illustrates the schematic of EO frequency comb generation in the PhC FP micro-resonator. A continuous-wave (CW) pump laser is coupled into the FP cavity through a partially transmitting PhC mirror, which serves as the input coupler.[35,36] The light then propagates along a folded U-shaped waveguide, reflects off a high-reflectivity PhC mirror at the end, and returns along the same path, forming standing-wave resonances. This folded geometry enables a long optical interaction length within a compact footprint, yielding a free spectral range (FSR) of 11 GHz. Push-pull electrodes induce opposite EO phase shifts in each arm of the waveguide, ensuring phase matching between the microwave drive and the optical modes. When the microwave frequency matches the FSR, efficient cascaded EO modulation occurs, generating a broadband and coherent EO frequency comb.[9,10]

The PhC reflectors are engineered to provide high reflectance and a tailored phase response only within the photonic bandgap, thereby defining the spectral window hosting high-Q cavity modes. As shown conceptually in Fig. 1b and quantitatively in Fig. 1c, the designed mirror exhibits a near-flat high-reflectance plateau ($R \approx 1$) across the target band, while wavelengths outside the bandgap experience reduced reflectance and rapidly decreasing cavity Q. Under the waveguide propagation loss of 1 dB m^{-1}, and a 6 mm round-trip length, we estimate the intrinsic quality factor to exceed 10^6 throughout the bandgap but to fall below 10^4 in the vicinity of Raman-active branches located outside the bandgap. This bandgap-based rejection prevents the formation of high-Q modes at Raman wavelengths and thus raises the threshold for stimulated Raman scattering (SRS), in contrast to approaches that rely on FSR detuning or coupling-loss engineering.

Another key advantage of our platform for EO frequency comb generation is the spontaneous formation of a zero-dispersion point, owing to the wavelength-dependent, non-trivial phase shift imparted by the PhC mirrors. Red-detuning from the bandgap center increases the field penetration into the mirror, effectively lengthening the round-trip path and reducing the FSR (anomalous-dispersion tendency). Blue-detuning has the opposite effect (normal-dispersion tendency). Consequently, the bandgap center marks a transition where the FSR is stationary with respect to wavelength, i.e., the group-velocity dispersion $\boldsymbol{D_2 \sim 0}$, yielding a natural zero-dispersion wavelength without additional compensators.

Figure 1d presents the integrated dispersion, $\boldsymbol{D_{\mathrm{int}} = \omega_\mu - (\omega_0 + \mu D_1)}$, which quantifies the deviation of the resonance frequencies from a perfectly equidistant grid. Here $\boldsymbol{D_1}$ is the FSR in rad s^{-1} and $\boldsymbol{\mu}$ indexes modes relative to the pumped mode. We calculate $\boldsymbol{D_{\mathrm{int}}}$ from the combined phase response of the PhC reflectors, designed such that the zero-dispersion point occurs at a wavelength of 1550 nm, and the 5.5 mm-long waveguide. A convex profile of $\boldsymbol{D_{\mathrm{int}}}$ corresponds to anomalous dispersion, while a concave profile indicates normal dispersion. Across waveguide widths ranging from 1 μm to 3 μm, the PhC-induced dispersion dominates over the waveguide contribution, enabling robust dispersion control through the PhC mirror design alone.

We numerically simulated EO comb evolution using a Heisenberg-picture model governed by the EO interaction Hamiltonian: $\boldsymbol{H_{EO} = \hbar g \sum_\mu \left(\hat{a}_{\mu+1}^\dagger \hat{a}_\mu \hat{b} + \hat{a}_{\mu-1}^\dagger \hat{a}_\mu \hat{b} + c.c\right)}$. Here, $\boldsymbol{\hat{a}_\mu}$ and $\boldsymbol{\hat{b}}$ represent the optical and microwave modes, respectively. In the simulation, we set the EO coupling strength $\boldsymbol{g/2\pi}$, which depends on the amplitude of the microwave drive and its spatial mode overlap with the optical field, to 2 GHz. We use an FSR of 10 GHz, yielding a modulation index $\boldsymbol{\beta = g/FSR = 0.4\pi}$. Using the spectral Q-factor distribution and the integrated dispersion profile from Figures 1c and 1d, respectively, we calculate the time-dependent evolution of the optical field under the Heisenberg equation of motion.

Figures 1e–1g show the simulated EO comb spectra for three representative pump wavelengths: 1540 nm, 1550 nm, and 1560 nm. At 1540 nm (Figure 1e), although the pump remains in the proximity of the photonic bandgap center, it is blue-detuned from the zero-dispersion point. In this regime, non-negligible phase mismatch arises as the integrated dispersion exceeds the modulation strength (*i.e.*, $\boldsymbol{|D_{\mathrm{int}}/2\pi| > g}$), limiting comb growth. On the other hand, at 1560 nm

(Figure 1g), although the dispersion remains favorable, red-detuned pumping brings the comb closer to the band edge, where degradation of the Q factor suppresses sideband formation according to the optical power drop given by $\boldsymbol{P_{\mu+1} = P_{\mu} e^{-\frac{\kappa}{2g}}}$.[10] At 1550 nm (Figure 1f), where both high Q factors and near-zero dispersion are simultaneously satisfied, efficient cascaded modulation yields broadband EO comb formation.

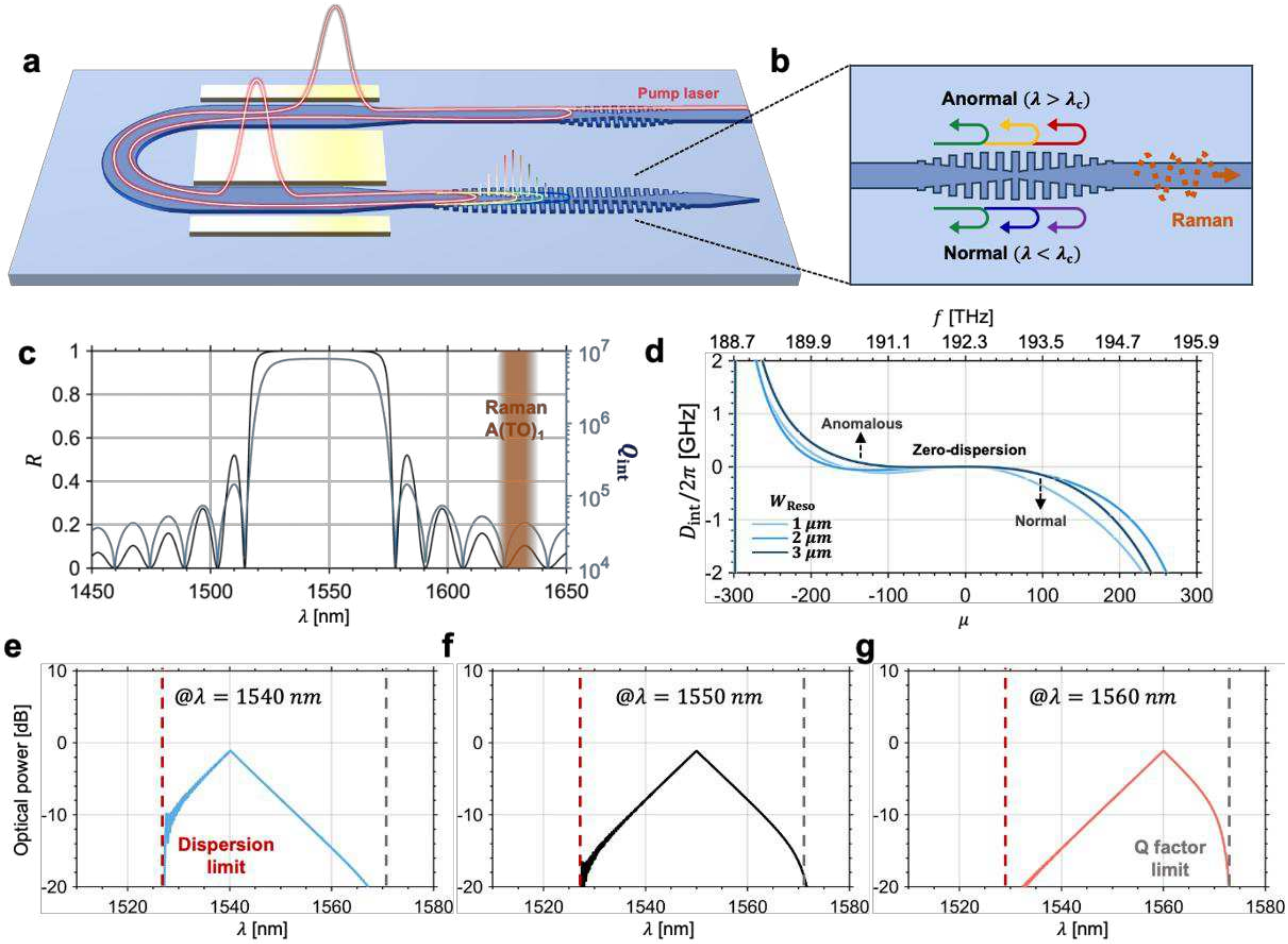


Fig. 1 (a) Schematic of the EO frequency comb based on the TFLN PhC FP micro-resonator. (b) Wavelength-selective reflectance and phase response of the PhC reflector. (c) Simulated reflectance (black) and intrinsic Q factor (blue), showing suppression near the Raman wavelength outside the bandgap. (d) Calculated integrated dispersion (D_{int}) of the PhC FP resonator for different waveguide widths, designed to yield a zero-dispersion point at 1550 nm. (e–g) Simulated EO comb spectra for pump wavelengths of 1540 nm, 1550 nm, and 1560 nm, showing dispersion-limited, ideal broadband, and Q-limited operation, respectively.

3. Fabrication and optical characterization of the PhC-FP EO microresonator

Figure 2a presents an optical microscope image of the fabricated PhC-FP microresonator**.** The device consists of a PhC input coupler, a 2.5-mm-long electro-optic modulation section, and a terminating high-reflectivity PhC reflector. The reflector and coupler share the same structural platform: a central PhC region sandwiched between tapered apodization sections.[35] The reflector includes 40 unit cells in its central PhC region to ensure high reflectance, while the coupler incorporates a single unit cell to promote efficient out-coupling of the generated sidebands under critical-coupling conditions. The tapered apodization section, spanning 30 unit cells, is incorporated between the waveguide and the central PhC region to minimize modal mismatch and insertion losses. Figure 2b shows scanning electron microscope (SEM) images of the PhC reflector and the EO modulation region. The PhC structure is patterned in a X-cut 490-nm-thick TFLN layer with a 300-nm etch depth and a 250-nm center width, and its corrugation width varies adiabatically from 0 nm in the apodization section to 700 nm in the central PhC region. The waveguide width from the PhC reflector/coupler to the modulation region is also adiabatically increased to reduce propagation loss caused by sidewall roughness.

Figures 2c and 2d present the measured resonant reflectance spectrum and the extracted Q-factor distributions, intrinsic (blue), coupling (purple), and loaded (black), across the tuning range of the external cavity diode laser, respectively. The experimental results show excellent agreement with calculations based on full 3D FDTD simulations (plotted as solid blue and purple lines in Figs. 2c and 2d). We extract Q factor by fitting reflection spectrum, with the frequency axis calibrated to a reference Mach-Zehnder Interferometer (MZI). The intrinsic Q factor exceeds 10^6 within the photonic bandgap, spanning ~650 resonant modes, but drops below 10^4 outside the bandgap, including the Raman-active spectral region.

The integrated dispersion $D_{\mathrm{int}} = \omega_\mu - (\omega_0 + \mu D_1)$ was experimentally extracted from the spectral distribution of the resonant modes. The FSR ($=D_1/2\pi$) near the zero-dispersion point was measured to be 11.90 GHz. Figure 2e plots the D_{int} profile relative to the resonant mode centered at 1550 nm. The smooth, monotonic trend without mode-splitting or avoided crossings indicates single mode operation in the fundamental TE_{00} mode. small ripples arise from weak end-facet reflections. To quantify the second-order dispersion D_2, the extracted D_{int} curve was fitted as a function of the mode number μ: $D_{\mathrm{int}} \sim \frac{1}{2}D_2\mu^2 + \frac{1}{6}D_3\mu^3 + \frac{1}{24}D_4\mu^4$. The zero-dispersion point (μ = 0) is observed near 1551 nm. The local second-order dispersion is computed by $D_2^\mu = \frac{d^2 D_{\mathrm{int}}}{d\mu^2} = D_2 + D_3\mu + \frac{1}{2}D_4\mu^2$, as shown in Figure 2e. Based on the location of the zero-dispersion point. the anomalous ($D_2^\mu > 0$) and normal ($D_2^\mu < 0$) dispersion regimes are distinguished for red- and blue-detuned modes, respectively.

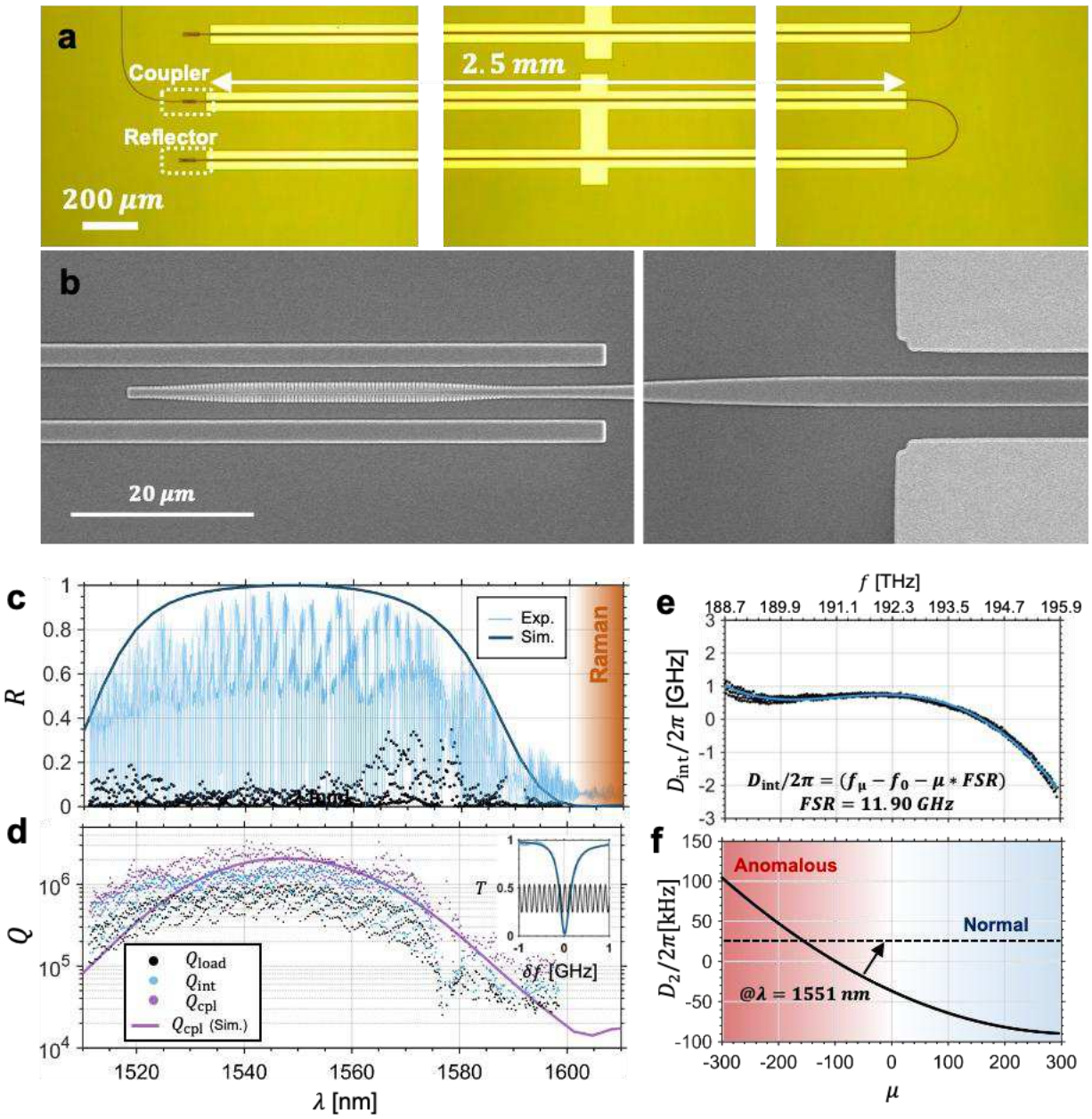


Fig. 2 (a) Optical microscope image of the fabricated device, comprising a PhC input coupler, a 2.5 mm-long EO modulation section, and a high-reflectivity PhC reflector. (b) SEM images of the PhC reflector and EO modulation section. The PhC corrugation and the waveguide width are adiabatically engineered to minimize optical losses. (c) Measured resonant reflectance spectrum (blue). Resonant minima are marked by black dots, and the dark blue line indicates the calculated reflectance of the PhC reflector. (d) Experimentally extracted Q-factor distributions—intrinsic (purple), coupling (blue), and loaded (dark green). The solid purple line indicates the simulated coupling Q-factor. Inset: Reflection spectrum of a representative resonant mode (blue) with a reference Mach–Zehnder interferometer (MZI) signal (black). (e) Experimentally extracted integrated dispersion (D_{int}) with respective to the resonant mode at 1550 nm. (f) Extracted second-order dispersion (D_2) from the polynomial fitting of D_{int} (solid blue line in (e)) as a function of the mode number μ. A zero-dispersion point is observed near 1551 nm, which distinguishes anomalous ($D_2 > 0$) and normal ($D_2 < 0$) dispersion regimes.

4. Experimental demonstration of EO frequency comb generation

Having characterized the dispersion and Q-factors of the PhC–FP cavity, we demonstrate EO frequency comb generation under resonant microwave driving conditions. Figure 3a shows the experimental setup used to generate and measure the EO frequency comb. A continuous-wave tunable laser is coupled into the PhC–FP cavity in the TE polarization state, passing through an erbium-doped fiber amplifier, optical attenuator, fiber polarization controller, and lensed fiber. The reflected signal is routed through an optical circulator to enable both spectral monitoring and active resonance locking via a servo-controller. The microwave drive signal is generated at a frequency matched to the cavity's FSR and amplified to 28 dBm before being applied to the on-chip ground–signal–ground (GSG) electrodes through a microwave circulator. The reflected microwave signal is absorbed using a 50-ohm impedance-matched load, and the optical comb output is collected from the circulator and analyzed using an optical spectrum analyzer.

Figure 3b presents the EO comb spectrum obtained at a pump wavelength of 1550 nm. The comb exhibits uniform spacing of 11.908 GHz, confirming phase-matched cascaded EO modulation. The on-chip optical pump power P_{chip} is 0.2 mW. It spans from 1544 to 1556 nm, yielding a bandwidth of ~12 nm, and shows a line-to-line power slope of ~0.8 dB per mode. Slight periodic modulations in the comb envelope are attributed to weak parasitic interference caused by end-facet reflections, which can be readily mitigated in future designs by applying anti-reflection coatings at the chip terminations. The red solid line in Fig. 3b shows the simulated spectral envelope of the EO comb, obtained by incorporating the experimentally measured Q-factor distribution into the Heisenberg-picture model. By fitting the simulated spectrum to the experimental result, we extract an effective EO modulation strength of $\boldsymbol{g}/2\pi$ = 1.67 GHz, corresponding to a modulation index of $\beta = 0.28\pi$. To explore the wavelength tunability of our EO comb generator, we swept the pump laser from 1530 nm to 1570 nm. As shown in Fig. 3c, EO combs were generated consistently, spanning the full photonic bandgap range from 1525 nm to 1572 nm.

Although the current device exhibits an intrinsic Q factor of approximately 10^6, which limits the present comb bandwidth, our platform can support full bandgap-spanning comb generation. This potential is demonstrated in the simulations shown in Figs. 1e–1g, which incorporate the calculated Q-factors well above 10^6 from Fig. 1c. The loaded Q-factor governs the cavity decay rate κ, and sideband power decays exponentially with increasing mode order (e.g., $P_{\mu+1}/P_{\mu} = e^{-\frac{\kappa}{2g}}$ for $\mu > 0$). As κ approaches the EO coupling strength g, energy transfer to outer lines becomes less efficient, reducing the observable comb span. The Q-factor can be increased by widening the central waveguide, which reduces scattering loss without significantly altering the FSR. Higher Q increases finesse, improving the cavity's ability to sustain cascaded modulation. The wavelength span of the comb is set by the EO coupling strength, finesse, and dispersion. Improved finesse enables EO combs that fully span the photonic bandgap.[9] In addition, EO coupling can be enhanced using microwave resonators for triple-resonance operation or photonic molecule designs to strengthen mode hybridization.[10]

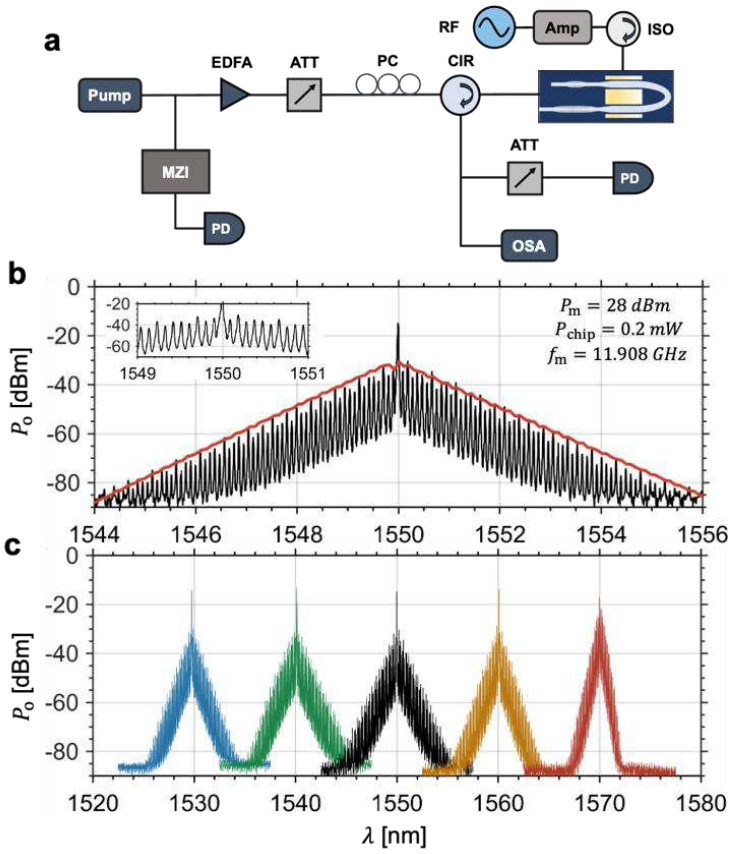


Fig. 3 (a) Schematic of the experimental setup for EO comb generation and measurement. ATT: optical attenuator; CIR: circulator; ISO: microwave isolator; MZI: Mach–Zehnder interferometer; PD: photodetector; OSA: optical spectrum analyzer. (b) EO comb spectrum measured with a 1550 nm pump (0.2 mW) and 11.908 GHz microwave drive (28 dBm). The comb shows uniform spacing, ~12 nm span, and a line-to-line power slope of ~0.04 dB/mode. The red line indicates the simulated spectrum fitted with an EO modulation strength of $g/2\pi = 1.67$ GHz. (c) Tunable EO combs measured while sweeping the pump wavelength from 1530 to 1570 nm.

5. EO Coupling strength and microwave detuning: Characterization and impact on comb dynamics

We comprehensively investigate EO comb generation in the PhC-FP micro-resonator as a function of the microwave drive power and frequency detuning. The EO coupling strength scales as $\boldsymbol{g = g_0\sqrt{n_m}}$, where $\boldsymbol{g_0}$ is the single-photon EO coupling strength and $\boldsymbol{n_m}$ is the number of microwave photons.[10] As the microwave power increases, both the EO intermode coupling and the magnitude of mode splitting in the reflection spectrum are enhanced. Figure 4a shows EO comb spectra at microwave powers (after amplifier) of 18 dBm, 23 dBm, and 29 dBm. The spectral bandwidth expands with increasing microwave power, as higher-order sidebands emerge due to stronger EO interaction. We measure the reflection spectrum of the resonance mode used for optical pumping in EO comb generation and observe increasing mode splitting with microwave power (Fig. 4b). At the microwave power of 29 dBm, the mode splitting, approximately twice the EO coupling strength, reaches ~2.98 GHz. Figure 4c presents the extracted EO coupling strength as a function of microwave power, showing good agreement with the theoretical square-root scaling.

We next explored the effect of microwave frequency detuning, $\boldsymbol{\Delta f_m = FSR - f_m}$, on comb formation at two distinct pump wavelengths: 1530 nm (normal dispersion) and 1550 nm (near the zero-dispersion point). As shown in Figs. 4d and 4e, both the bandwidth and spectral symmetry of the generated combs are highly sensitive to $\boldsymbol{\Delta f_m}$. When the microwave frequency is detuned from the cavity's FSR, phase mismatch reduces the effective coupling and limits the comb span. Quantitatively, EO comb formation is restricted to regions where $\boldsymbol{|D_{int}/2\pi| < g}$. In Figs. 4f and 4g, we extract $\boldsymbol{D_{int}}$ relative to an equidistant frequency grid defined by $\boldsymbol{f_m}$, based on the measured EO comb spectra in Figs. 4d and 4e. Indeed, the range of $\boldsymbol{D_{int}}$ (white region in Figs. 4f and 4g), defined by the measured coupling strength $\boldsymbol{g}$ ≈ 1.49 GHz in Fig. 4b, determines the spectral extent of the EO comb span. This agreement confirms the notable consistency between the EO coupling strength obtained from direct mode-splitting measurement and that estimated from the comb bandwidth.

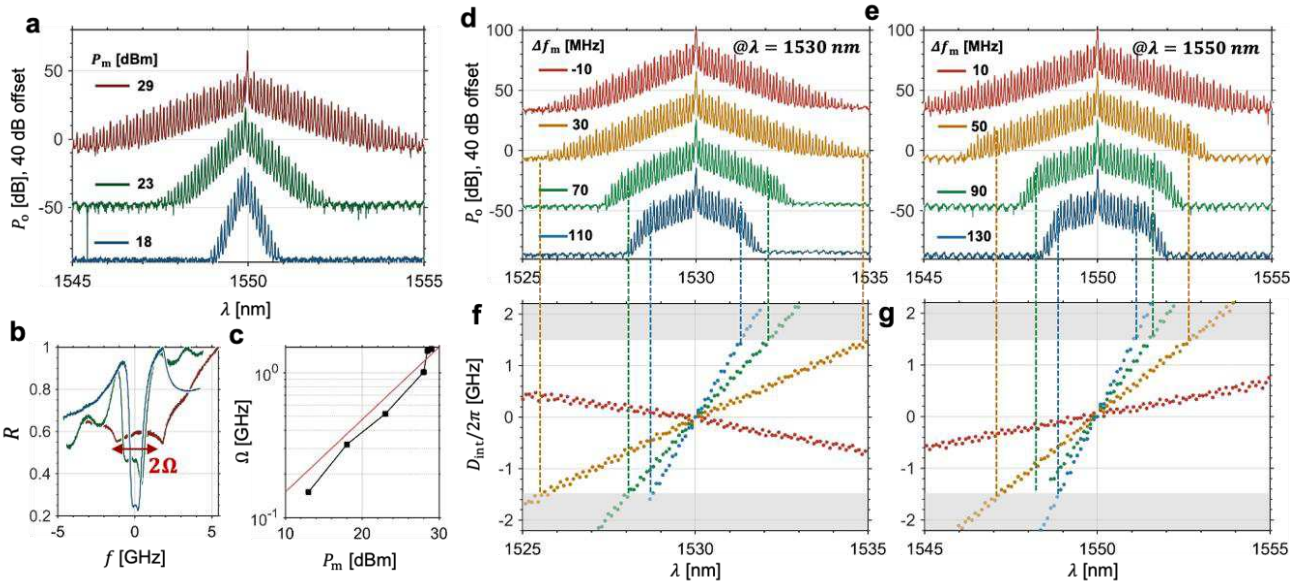


Fig. 4 (a) EO comb spectra measured at on-chip microwave powers of 18, 23, and 29 dBm (1550 nm pump). (b) Reflection spectra of the resonance mode used for optical pumping, showing increasing mode splitting with microwave power. (c) Extracted EO coupling strength g as a function of on-chip microwave power, exhibiting square-root dependence (solid red line). (d, e) EO comb spectra as a function of microwave frequency detuning Δf_m, measured at pump wavelengths of 1530 nm (normal dispersion) and 1550 nm (near the zero-dispersion point), respectively. (f, g) Integrated dispersion extracted from EO comb spectra in (d) and (e), plotted relative to the microwave frequency grid defined by f_m. The white region denotes the range $|D_{\mathrm{int}}/2\pi| < g$, consistent with the measured coupling strength g ≈ 1.49 GHz from (b).

6. Exclusion of stimulated Raman scattering

To realize exclusion of stimulated Raman scattering, we operated the device under high optical pump powers. As discussed earlier, the intrinsic Q-factor is on the order of 10^6 within the photonic bandgap but drops below 10^4 near the spectral region of the transverse optical A1-mode Raman branch expected around 1625 nm, thereby preventing cavity enhancement of Raman signals. Figure 5 shows EO comb spectra measured at on-chip pump powers of 20 mW and 200 mW. In both cases, no Stokes signals appear near 1625 nm, confirming effective exclusion of TO A_1-mode Raman scattering by the photonic bandgap. Even at 200 mW, the background spectral intensity in this region remains unchanged and indicate no stimulated Raman signal above the detection noise floor. These measurements set an upper bound on Raman conversion at the device output at least 80 dB below the pump-referenced level, and therefore validate that bandgap-based spectral exclusion, rather than FSR detuning or coupling-loss engineering, is sufficient to prevent Raman-assisted comb growth.

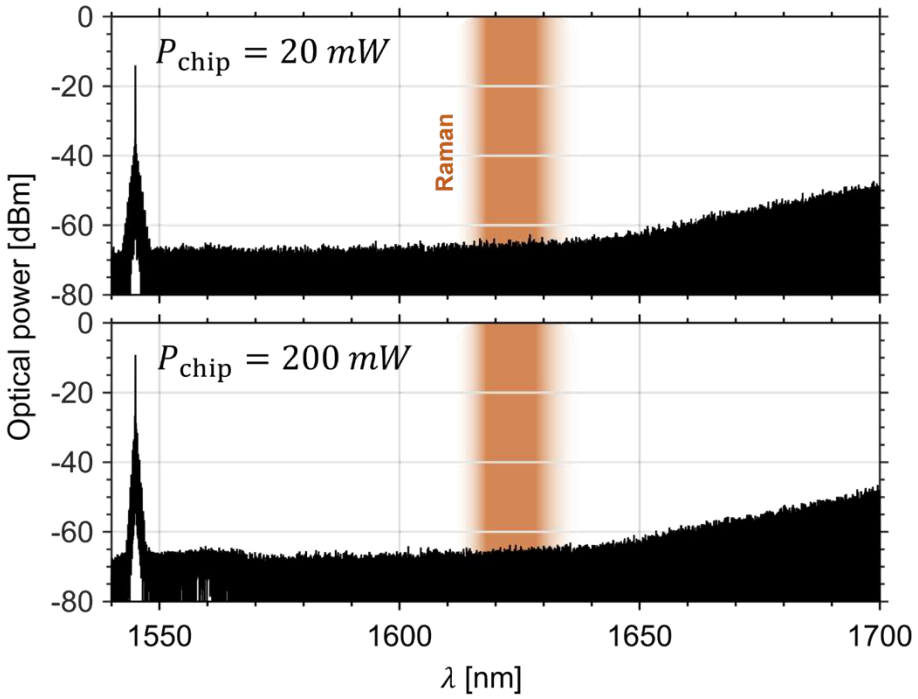


Fig. 5 EO comb spectra measured at on-chip pump powers of 20 mW and 200 mW, showing no Stokes signals near 1625 nm. The absence of spectral features in this region confirms effective exclusion of TO A_1-mode Raman scattering outside the photonic bandgap, even under strong optical excitation.

7. Conclusion

We have demonstrated an EO frequency-comb platform based on a dispersion-engineered PhC-FP micro-resonator in thin-film lithium niobate that simultaneously provides a high-Q passband for standing-wave modes and intrinsic spectral exclusion of Raman-susceptible regions. The phase response of the PhC mirror provides a natural zero-dispersion point within the photonic bandgap region. Using this unique architecture, we generated coherent EO combs with FSR-locked spacing and verified wavelength tunability by sweeping the pump across the photonic bandgap without retuning the RF frequency. Quantitatively, the EO coupling rate extracted from both mode-splitting and detuning-dependent spectral analysis agrees and follows the expected square-root scaling of the optical power depending on the on-chip microwave power ($g/2\pi \approx 1.5{-}1.7$ GHz), while the simple design rule, $|D_{\mathrm{int}}/2\pi| < g$, accurately predicts comb bandwidth and symmetry under RF detuning and pump repositioning. Particularly, we demonstrated Raman-free EO comb event at an on-chip operating optical power up to 200 mW.

Beyond establishing a compact and programmable EO-comb source, our results also provide clear knobs and guidelines for scaling: (i) raise finesse by reducing scattering loss (e.g., wider central waveguides, surface treatment, AR-coated facets); (ii) increase g via microwave-resonator co-design or photonic-molecule coupling; and (iii) tailor D_{int} through PhC mirror dispersion to place the zero-dispersion point at a target operating wavelength. These knobs point to bandgap-spanning, low-phase-noise EO combs well-suited for coherent communications, agile frequency synthesis, and quantum-photonic systems.

8. Acknowledgments

9. Funding

M.K.S and H.L acknowledge support by KAIST Cross-Generation Collaborative Lab project. the Institute for Information, Communication Technology Promotion of Korea (2021-0-00552), the National Research Foundation of Korea (RS-2024-00350185, RS-2024-00408271), the National Research Council of Science and Technology (CAP21034-000, GTL25011-102).

10. Conflict of Interest

The authors have no conflicts to disclose.

11. Author Contributions

HYEON HWANG led the conceptualization, investigation, data curation, formal analysis, visualization, and writing of the original draft, and contributed equally to review and editing. Seokjoo Go contributed equally to data curation, formal analysis, and review and editing. Guhwan Kim, Hong-Seok Kim, Kiwon Moon, and Jung Jin Ju contributed to the investigation, resources, and review and editing. Hansuek Lee and Min-Kyo Seo contributed equally to funding acquisition, project administration, and supervision, and contributed equally to original draft preparation and review and editing.

12. Data availability

The data that support the findings of this study are available from the corresponding author upon reasonable request.

13. References

1. Fortier, T. & Baumann, E. 20 years of developments in optical frequency comb technology and applications. *Commun. Phys.* **2**, 153; doi:10.1038/s42005-019-0249-y (2019).
2. Diddams, S. A., Vahala, K. & Udem, T. Optical frequency combs: Coherently uniting the electromagnetic spectrum. *Science* **369**, 267–272; doi:10.1126/science.aay3676 (2020).
3. Chang, L., Liu, S. & Bowers, J. E. Integrated optical frequency comb technologies. *Nat. Photonics* **16**, 95–108; doi:10.1038/s41566-021-00945-1 (2022).
4. Corcoran, B., Mitchell, A., Morandotti, R., Oxenløwe, L. K. & Moss, D. J. Optical microcombs for ultrahigh-bandwidth communications. *Nat. Photonics* **19**, 451–462; doi:10.1038/s41566-025-01662-9 (2025).
5. Lukashchuk, A. et al. Photonic-electronic integrated circuit-based coherent LiDAR engine. *Nat. Commun.* **15**, 123; doi:10.1038/s41467-024-00000-x (2024).
6. Rueda, A., Sedlmeir, F., Kumari, M., Leuchs, G. & Schwefel, H. G. L. Resonant electro-optic frequency comb. *Nature* **568**, 378–381 (2019).
7. Zhang, M., Wang, C., Kharel, P., Zhu, D. & Lončar, M. Integrated lithium niobate electro-optic modulators: when performance meets scalability. *Optica* **8**, 652 (2021).
8. Zhang, K. et al. A power-efficient integrated lithium niobate electro-optic comb generator. *Commun. Phys.* **6**, 145; doi:10.1038/s42005-023-01234 (2023).
9. Zhang, M. et al. Broadband electro-optic frequency comb generation in a lithium niobate microring resonator. *Nature* **568**, 373–377 (2019).
10. Zhang, J. et al. Ultrabroadband integrated electro-optic frequency comb in lithium tantalate. *Nature* **637**, 1096–1103 (2025).
11. Zhu, D. et al. Integrated photonics on thin-film lithium niobate. *Adv. Opt. Photon.* **13**, 242 (2021).
12. Saravi, S., Pertsch, T. & Setzpfandt, F. Lithium niobate on insulator: an emerging platform for integrated quantum photonics. *Adv. Opt. Mater.* **9**, 2101234 (2021).
13. Zhao, J., Ma, C., Rüsing, M. & Mookherjea, S. High quality entangled photon pair generation in periodically poled thin-film lithium niobate waveguides. *Phys. Rev. Lett.* **124**, 163603 (2020).
14. Hwang, H. et al. Electro-optic control of the external coupling strength of a high-quality-factor lithium niobate micro-resonator. *Opt. Lett.* **47**, 6149 (2022).
15. Wang, C. et al. Monolithic lithium niobate photonic circuits for Kerr frequency comb generation and modulation. *Nat. Commun.* **10**, 978 (2019).
16. Wang, C., Zhang, M., Stern, B., Lipson, M. & Lončar, M. Nanophotonic lithium niobate electro-optic modulators. *Opt. Express* **26**, 1547 (2018).
17. Boes, A. et al. Lithium niobate photonics: unlocking the electromagnetic spectrum. *Science* **379**, 4396; doi:10.1126/science.abj4396 (2023).
18. Chen, G. et al. Advances in lithium niobate photonics: development status and perspectives. *Adv. Photon.* **4**, 034003; doi:10.1117/1.AP.4.3.034003 (2022).
19. Li, M. et al. Lithium niobate photonic-crystal electro-optic modulator. *Nat. Commun.* **11**, 4123 (2020).
20. Stokowski, H. S. et al. Integrated quantum optical phase sensor in thin film lithium niobate. *Nat. Commun.* **14**, 456 (2023).
21. Lu, J., Li, M., Zou, C.-L., Al Sayem, A. & Tang, H. X. Toward 1% single-photon anharmonicity with periodically poled lithium niobate microring resonators. *Optica* **7**, 1654 (2020).
22. Hwang, H. et al. Spontaneous parametric down-conversion photon pair generation in small footprint X-cut periodically poled lithium niobate micro-resonator. *Opt. Lett.* **49**, 3039; doi:10.1364/OL.533039 (2024).
23. Hwang, H. et al. A wide-spectrum mid-infrared electro-optic intensity modulator employing a two-point coupled lithium niobate racetrack resonator. *APL Photon.* **10**, 012345 (2025).
24. Hwang, H. et al. Hyperband electro-optic modulator based on a two-pulley coupled lithium niobate racetrack resonator. *Opt. Lett.* **49**, 658 (2024).
25. Song, Y. et al. Universal dynamics and microwave control of programmable cavity electro-optic frequency combs. *Preprint*; doi:10.48550/arXiv.2501.12345 (2025).
26. Lei, T. et al. Strong-coupling and high-bandwidth cavity electro-optic modulation for advanced pulse-comb synthesis. *Preprint*; doi:10.48550/arXiv.2502.67890 (2025).
27. Fan, H. et al. Photon conversion in thin-film lithium niobate nanowaveguides: a noise analysis. *J. Opt. Soc. Am. B* **38**, 2172 (2021).
28. Nie, B. et al. Soliton microcombs in X-cut $LiNbO_3$ microresonators. *eLight* **5**, 23 (2025).
29. Song, Y., Zhu, X., Zuo, X., Huang, G. & Lončar, M. Stable gigahertz- and mmWave-repetition-rate soliton microcombs on X-cut lithium niobate. *Optica* **12**, 693 (2025).
30. Wan, S. et al. Self-locked broadband Raman-electro-optic microcomb. *Nat. Commun.* **16**, 1234 (2025).
31. Yu, M. et al. Raman lasing and soliton mode-locking in lithium niobate microresonators. *Light Sci. Appl.* **9**, 9 (2020).
32. Zhao, Y., Liu, X., Yvind, K., Cai, X. & Pu, M. Widely-tunable, multi-band Raman laser based on dispersion-managed thin-film lithium niobate microring resonators. *Commun. Phys.* **6**, 123 (2023).
33. Song, Y., Hu, Y., Zhu, X., Yang, K. & Lončar, M. Octave-spanning Kerr soliton frequency combs in dispersion- and dissipation-engineered lithium niobate microresonators. *Light Sci. Appl.* **13**, 12 (2024).

34. Lv, X. et al. Broadband microwave-rate dark pulse microcombs in dissipation-engineered $LiNbO_3$ microresonators. *Nat. Commun.* **16**, 4567 (2025).
35. Hwang, H. et al. High-Q photonic crystal Fabry-Perot micro-resonator in thin-film lithium niobate. *Preprint* (2025).
36. Seo, M.-K. et al. Photonic molecules via coupled thin-film lithium niobate Fabry-Pérot photonic crystal micro-resonators. *Optica Open*; doi:10.1364/opticaopen.30092995.v1 (2025).